

Diff-FMT: Diffusion Models for Fluorescence Molecular Tomography

Qianqian Xue^{1#}, Peng Zhang^{1#}, Xingyu Liu¹, Wenjian Wang^{1*}, Guanglei Zhang^{2*}

¹School of Computer and Information Technology, Shanxi University, Taiyuan 030006, China

²School of Biological and Medical Engineering, Beihang University, Beijing 100191, China

wjwang@sxu.edu.cn, guangleizhang@buaa.edu.cn

Abstract

Fluorescence molecular tomography (FMT) is a real-time, noninvasive optical imaging technology that plays a significant role in biomedical research. Nevertheless, the ill-posedness of the inverse problem poses huge challenges in FMT reconstructions. Previous various deep learning algorithms have been extensively explored to address the critical issues, but they remain faces the challenge of high data dependency with poor image quality. In this paper, we, for the first time, propose a FMT reconstruction method based on a denoising diffusion probabilistic model (DDPM), termed Diff-FMT, which is capable of obtaining high-quality reconstructed images from noisy images. Specifically, we utilize the noise addition mechanism of DDPM to generate diverse training samples. Through the step-by-step probability sampling mechanism in the inverse process, we achieve fine-grained reconstruction of the image, avoiding issues such as loss of image detail that can occur with end-to-end deep-learning methods. Additionally, we introduce the fluorescence signals as conditional information in the model training to sample a reconstructed image that is highly consistent with the input fluorescence signals from the noisy images. Numerous experimental results show that Diff-FMT can achieve high-resolution reconstruction images without relying on large-scale datasets compared with other cutting-edge algorithms.

Introduction

Fluorescence molecular tomography (FMT), as a non-invasive real-time optical molecular imaging technique, has been applied in many medical fields such as drug development (Willmann et. al. 2008; Stuker, Ripoll and Rudin 2011), early diagnosis of diseases (Li et. al. 2023; He et. al. 2024) and treatment monitoring (Ntziachristos et. al. 2002; Ntziachristos et. al. 2004) owing to its high sensitivity and high spatial resolution (Han et. al. 2021). However, due to the strong scattering effect of biological tissues and limited surface measurement data, the FMT reconstruction suffers from severe ill-posedness. Therefore, it is of great significance to enormously alleviate the ill-posedness of its inverse problem to improve the FMT reconstruction performance.

Previously, researchers have proposed a variety of reconstruction algorithms, one of the most representative of which is the traditional iteration-based regularization method. They

primarily alleviate the ill-posedness of the inverse problem by introducing regularization conditions or and incorporating sparse prior knowledge, mainly including Tikhonov and sparse regularization. Tikhonov regularization suppresses image artifacts by introducing L2 norms (Cheng, and Luo 2020), but this type of regularization term may lose image information and make the image too smooth. Sparse regularization methods typically constrain the fluorescent source through L1 and L0 norms (Xie et. al. 2014; Yuan et. al. 2023), which can ensure the sparsity of the solution while preserving the high-frequency information, but may lead to problems of over-sparse and information missing. To overcome the above-mentioned problems, researchers have proposed other regularization algorithms to simulate the sparsity of fluorescence signals, such as L1-L2 differential regularization (Luo et. al. 2023), elastic regularization (Chen et. al. 2023), and group sparse regularization (Wu et. al. 2024), etc. However, these algorithms heavily rely on the selection of hyperparameters, and suffer from long reconstruction time and low solution efficiency.

In recent years, deep learning has been widely applied in the field of FMT, primarily focusing on data-driven deep learning reconstruction FMT methods. These methods require constructing a nonlinear mapping relationship between fluorescence signals and reconstructed images through end-to-end deep networks. Guo et. al. (2019) proposed an three-dimensional (3D) encoder-decoder network to achieve the fast reconstruction of FMT. Meng et. al. (2020) first used a k-nearest neighbor fully connected sub-network to obtain preliminary fluorescence images, and then used a locally connected sub-network for morphological fine-tuning to achieve morphological reconstruction. Zhang et. al. (2021) proposed a 3D fused dual-sampling convolutional neural network that can eliminate modeling errors while significantly improving spatial resolution. Cao et. al. (2022) developed a fully-connected network model to simulate the back propagation process of photons and improved the FMT reconstruction accuracy by incorporating the center of gravity error in the loss function. Zhang et. al. (2023) used only four vertical projection views and two convolutional networks to solve the

sparse view reconstruction problem. Overall, the data-driven deep learning algorithm can effectively overcome the problems of long reconstruction time and low spatial resolution of traditional algorithms. However, training network models requires a large amount of high-quality paired data, usually tens of thousands, and the reconstruction results are heavily dependent on the quality of the dataset. Especially when the dataset quality is poor, it is difficult to obtain good reconstruction results.

Recently, model-driven deep learning methods have also been gradually used for FMT reconstruction. Model-driven deep learning algorithms usually unfold the iterative algorithms process into a deep network and implement FMT reconstruction under the condition of domain prior knowledge. Hua et. al. (2022) unfolded the projected gradient descent algorithm into a deep network, and obtained high-quality images with only a few hundred training samples. Sun et. al. (2024) introduced nonnegative prior information into algebraic reconstruction (ART) and used residual convolutional neural network as a corrector to improve image accuracy. Yang et. al. (2022) combined the Iterative Shrinkage Thresholding Algorithm (ISTA) with the U-Net network and proposed an interpretable ISTA-UNet algorithm to improve image quality. Jiang et. al. (2023) combined FISTA with a 3D convolutional module to automatically learn deep background modeling error to improve the image accuracy. Liu et. al. (2023) proposed a spatially adaptive split Bregman network (SSB-Net) to overcome the limitations of spatial non-uniformity in measurement sensitivity, and achieved the high-fidelity FMT. In general, model-driven deep learning methods can improve model performance using relatively few training samples, but the computational complexity is relatively large and the requirements for physical models are high. Therefore, there is an urgent need to propose a new reconstruction algorithm that does not rely on large datasets, complex models and computational complexity and can significantly improve the quality of FMT reconstruction.

The diffusion model (Ho, Jain, and Abeel 2020) is an emerging generative model. Different from the pixel-by-pixel feature extraction of CNN and the global attention of Transformer, the diffusion model has performed well in the field of medical imaging owing to its unique forward diffusion-inverse denoising iterative process. Firstly, the noise phase of the diffusion model can not only generate diverse samples to increase the amount of data, but also simulate a variety of interference factors in the process of medical image acquisition through noise. Secondly, each step of the inverse stage of the diffusion model generates an image by estimating the probability of data distribution, which can not only learn the essential characteristics of the image step by step, but also significantly enhance the interpretability of the model, so that the model can obtain better results with limited information. In view of the powerful performance of the dif-

fusion model, we, for the first time, propose an FMT reconstruction algorithm based on the denoising diffusion probabilistic model (DDPM), called Diff-FMT. Specifically, we extend DDPM as a network framework suitable for FMT reconstruction. In the training phase, we input the measured fluorescence signals as conditional information into the U-shaped network together with the real fluorescence images. In the sampling stage, we start from random noise and obtain the corresponding high-quality fluorescence images under the conditions of given fluorescence signals. The main contributions of this paper are as follows:

- We make the first attempt to combine the DDPM with optical imaging to achieve high-quality FMT reconstruction. Unlike previous CNNs that focus on pixel-by-pixel feature extraction and Transformer that emphasize global context, Diff-FMT leverages a unique noise addition-denoising mechanism to obtain reconstructed fluorescence images through stepwise probabilistic sampling.
- We add fluorescence signal as a condition in the model training stage of Diff-FMT, and implicitly establish the relationship between the fluorescence signal and the real image by using U-network, which makes it possible to obtain the corresponding high-quality 3D reconstructed image from the noise for a given fluorescence signal at the time of sampling.
- We propose the first diffusion model-based 3D image reconstruction network. Compared with other CNN or Transformer networks, the Diff-FMT does not need to rely on large-scale training datasets and can gradually recover high-quality 3D reconstruction images from random noise using a small dataset.

The rest of the paper is organized as follows. We introduce the proposed Diff-FMT method in Section 2, present the experimental setup and results in Section 3, and conclude in Section 4.

Methodology

Forward and Inverse Problems in FMT

Traditional FMT includes forward and inverse problems. The forward problem mainly describes the complex propagation process of light in biological tissues by establishing a coupled diffusion equation. In a continuous-wave FMT imaging system, the propagation process of excitation light and fluorescence (Han et. al. 2010) can be described as:

$$\begin{cases} \nabla \cdot (D_x(r) \nabla \Phi_x(r)) - \mu_{ax}(r) \Phi_x(r) = -\Theta \delta(r - r_i) \\ \nabla \cdot (D_m(r) \nabla \Phi_m(r)) - \mu_{am}(r) \Phi_m(r) = -\Phi_x(r) \eta \mu_{af}(r) \end{cases} \quad (r \in \Omega) \quad (1)$$

where r is the position vector, ∇ is the gradient operator, x and m represent the excitation and fluorescence wavelengths, respectively. Φ_x and Φ_m represent the photon densities of the excitation and fluorescence, $\delta(r - r_i)$ represents the excitation source, $D_{x,m}$ and $\mu_{ax,am}$ represent the diffusion coeffi-

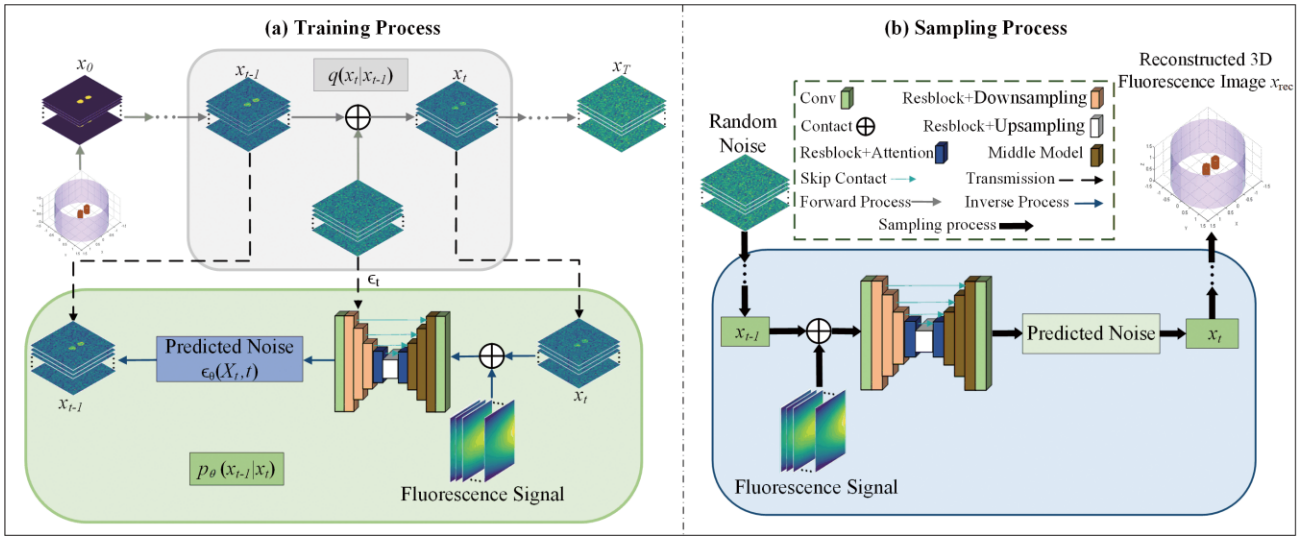


Figure 1: Overview of the Diff-FMT algorithm. Diff-FMT includes: (a) Training phase and (b) Sampling phase. The training phase includes: (a1) Forward process $q(x_t | x_{t-1})$ and (a2) Inverse process $p_\theta(x_{t-1} | x_t)$.

cients and the absorption coefficients, respectively. Θ represents the position of the point excitation source, and $\eta\mu_{df}(r)$ represents the fluorescence yield to be reconstructed.

Combining the Robin-type boundary conditions (Soubret, Ripoll, and Ntziachristos 2005) and using the finite element method (Zhang et. al. 2015a) to solve equation (1), we obtain the following coupling matrix equation:

$$\begin{aligned} K_x \Phi_x &= S_x \\ K_m \Phi_m &= Fx \end{aligned} \quad (2)$$

where K_x and K_m are the system matrices, S_x is the excitation source vector. F is the matrix obtained by discretizing the fluorescence yield distribution, and x represents the reconstructed fluorophore. The inverse problem can be obtained by solving equation (2):

$$\Phi = Wx \quad (3)$$

where W is a system matrix describing the relationship between the fluorescence image to be reconstructed x and the surface fluorescence measurement signals Φ . In previous studies, equation (3) is usually transformed into a minimization problem with a regularization term (Guo et. al. 2015) to find an approximate solution:

$$\min_x \left\{ \frac{1}{2} \| Wx - \Phi \|_2^2 + \alpha R(x) \right\} \quad (4)$$

where α is the parameter that balances the data term and the regularization term, and $R(x)$ is the regularization term. Although traditional algorithms can improve the accuracy of reconstructed images, they suffer from longer reconstruction times, difficulty in parameter selection, reliance on prior knowledge, and can result in image smoothing, which degrades the reconstruction quality. Unlike traditional algorithms, deep learning algorithms usually train an end-to-end mapping network to establish the relationship between x and Φ (Zhang et. al. 2021):

$$x_{net} = f_{net}(\Phi_{net}) \quad (5)$$

where f_{net} is the constructed network model, Φ_{net} and x_{net} are the input and output of the network, respectively. The network is optimized by minimizing the difference between the network estimation data and the real fluorescence image. However, such end-to-end deep learning algorithms require a large number of training samples and prior knowledge, and when confronted with untrained data, the model may exhibit poor generalization ability, resulting in the reconstructed image still with unclear and non-separable fluorophore edges.

Diff-FMT for FMT Reconstruction

The network framework of the Diff-FMT is shown in Figure 1. Its training process is the same as the that of diffusion model, including the forward process $q(x_t | x_{t-1})$ and inverse process $p_\theta(x_{t-1} | x_t)$. The forward process starts with the real image x_{ori} and gradually adds noise to obtain the Gaussian noise image x_t . In the inverse process, the reconstructed 3D image is obtained by introducing fluorescence signals as a condition of random noise. In the sampling stage, given the random noise and fluorescence signals, the trained model is used to generate a reconstructed image. The training process of Diff-FMT can be expressed as:

$$x_0 = x_{ori} \Leftrightarrow \dots \Leftrightarrow x_{t-1} \xrightarrow[q_\theta(x_t | x_{t-1})]{p_\theta(x_{t-1} | x_t, \Phi_c)} x_t \Leftrightarrow \dots \Leftrightarrow x_T \quad (6)$$

where x_1, \dots, x_T is a latent variable of the same size as x_0 , Φ_c is the introduced fluorescence signals, and $q(\cdot)$ and $p_\theta(\cdot)$ represent the forward and inverse processes of Diff-FMT, respectively.

Diffusion Forward Process

In the forward process, Gaussian noise with variance β_1, \dots, β_T is gradually added to the real image $x_0 = x_{ori}$ to obtain a series of noise-added images x_1, \dots, x_T . The latent variable x_t

Algorithm 1: Training Algorithm

Input: Total steps T , Fluorescence signals and real images dataset $D = \{(\Phi_c^i, x_{ori}^i)\}_{i=1}^N$

- 1: **repeat**
 - 2: sample $t \sim \text{Uniform}(1, \dots, T)$
 - 3: sample $(\Phi_c^i, x_{ori}^i) \sim D, \epsilon_t \sim N(0, \mathbf{I})$
 - 4: $X_t = \Phi_c \oplus x_t$
 - 5: Take gradient step on
 - 6: $E_{x_t, \epsilon_t, t} [\|\epsilon_t - \epsilon_\theta(X_t, t)\|^2], x_t = \sqrt{\bar{\alpha}_t} x_{ori}^i + \sqrt{(1 - \bar{\alpha}_t)} \epsilon_t$
 - 7: **until** convergence
-

and the probability distribution it obeys in step t are denoted respectively:

$$x_t = \sqrt{1 - \beta_t} x_{t-1} + \sqrt{\beta_t} \epsilon_t, \epsilon_t \sim N(0, \mathbf{I}) \quad (7)$$

$$q(x_t | x_{t-1}) = \mathcal{N}(x_t; \sqrt{1 - \beta_t} x_{t-1}, \beta_t \mathbf{I}) \quad (8)$$

where ϵ_t is the random noise added at step t and \mathbf{I} is an $n \times n$ dimensional unit matrix. The forward process can be viewed as a Markov chain, denoted as:

$$q(x_t | x_0) = \prod_{i=1}^t q(x_i | x_{i-1}) = \mathcal{N}(x_t; \sqrt{\bar{\alpha}_t} x_{ori}, (1 - \bar{\alpha}_t) \mathbf{I}) \quad (9)$$

$$\beta_t = \beta_1 + \frac{t(\beta_T - \beta_1)}{T - 1} \quad (10)$$

where $1 \leq t \leq T$, $x_T \sim N(0, \mathbf{I})$ is a purely noisy image. $\alpha_t = 1 - \beta_t$ and $\bar{\alpha}_t = \prod_{m=1}^t \alpha_m$. β_1, \dots, β_T increases linearly from $\beta_1 = 10^{-4}$ to $\beta_T = 2^* 10^{-2}$ according to equation (10). By reparameterization, equation (9) can be expressed as:

$$x_t = \sqrt{\bar{\alpha}_t} x_0 + \sqrt{(1 - \bar{\alpha}_t)} \epsilon_t, \epsilon_t \sim N(0, \mathbf{I}) \quad (11)$$

Therefore, in the forward process, we start from the FMT real image x_{ori} and obtain a series of noisy images and random noises through equation (11), which are stored in the image dataset $\{x_{ori}, x_1, x_2, \dots, x_T\}$ and the noise dataset $\{\epsilon_0, \epsilon_2, \epsilon_3, \dots, \epsilon_T\}$, respectively, in preparation for the model training in the inverse process.

Diffusion Inverse Processes

The general inverse process p starts with a random Gaussian noise image and gradually removes the noise to obtain an image close to the original data distribution (Ho, Jain, and Abbeel 2020). The process is generally represented as:

$$p(x_{t-1} | x_t, x_0) = \mathcal{N}(x_{t-1}; \mu_t(x_t, x_0), \tilde{\beta}_t \mathbf{I}) \quad (12)$$

$$\tilde{\beta}_t = \frac{1 - \bar{\alpha}_{t-1}}{1 - \bar{\alpha}_t} \beta_t \quad (13)$$

$$x_0 = \frac{1}{\sqrt{\bar{\alpha}_t}} (x_t - \sqrt{(1 - \bar{\alpha}_t)} \epsilon_t) \quad (14)$$

where $p(x_{t-1} | x_t, x_0)$ is the posterior probability distribution that the image obeys at moment $t-1$ given x_0 and x_t . Since x_0 is unknown in the inverse process, we compute x_0 by equation (14). But unlike the forward process, the noise ϵ_t to

Algorithm 2: Sampling Algorithm

Input: Total steps T , Fluorescence signals $\Phi_c, x_T \sim N(0, \mathbf{I})$

Output: x_{rec}

- 1: **for** $t = T, \dots, 1$ **do**
 - 2: $X_t = \Phi_c \oplus x_t$
 - 3: $z \sim N(0, \mathbf{I})$
 - 4: $x_{t-1} = \frac{1}{\sqrt{\alpha_t}} (x_t - \frac{1 - \alpha_t}{\sqrt{1 - \bar{\alpha}_t}} \epsilon_\theta(X_t, t)) + \tilde{\beta}_t^{\frac{1}{2}} z$
 - 5: **end for**
-

be removed at each step of the process is not known, so the noise value $\epsilon_\theta(x_t, t)$ at moment t is generally estimated by the neural network.

In Diff-FMT, the core goal of the inverse process is to obtain FMT reconstructed images that are close to the real fluorescence images from random noise. To achieve this goal, during the training process, we feed the fluorescence signals Φ_c as a conditional information into the model at each step along with the latent variables to predict the noise information to be removed at each step. The training process is shown in Algorithm 1. The specific steps are as follows:

First, we combine the fluorescence signals Φ_c (size (num, n, n)) and the latent variable x_t (size (c, n, n)) to obtain image X_t of size $(num + c, n, n)$:

$$X_t = \Phi_c \oplus x_t \quad (15)$$

where num is the number of excitation sources, i.e., the number of fluorescence signals, and c is the number of slices taken in the real image. For X_t , we only update x_t according to equation (11), while the conditional image Φ_c remains unchanged.

Then, we input X_t into the noise estimation model μ_θ , which employs a U-shaped network with residual blocks and temporal embedding modules (Ho, Jain, and Abbeel 2020). The loss function of the model is set as:

$$E_{x_t, \epsilon_t, t} [\|\epsilon_t - \epsilon_\theta(X_t, t)\|^2] \quad (16)$$

where ϵ_t comes from the noisy dataset constructed by the forward process and $\epsilon_\theta(X_t, t)$ is the noise information to be removed at each step. After obtaining $\epsilon_\theta(X_t, t)$, we can get the mean of the posterior distribution as:

$$\begin{aligned} \mu_\theta(X_t, t) &= \frac{\sqrt{\bar{\alpha}_{t-1}} \beta_t}{1 - \bar{\alpha}_t} x_0 + \frac{\sqrt{\alpha_t} (1 - \bar{\alpha}_{t-1})}{1 - \bar{\alpha}_t} x_t \\ &= \frac{1}{\sqrt{\alpha_t}} (x_t - \frac{\beta_t}{\sqrt{1 - \bar{\alpha}_t}} \epsilon_\theta(X_t, t)) \end{aligned} \quad (17)$$

According to equation (17), the posterior distribution that x_{t-1} obeys when x_t is known is:

$$p_\theta(x_{t-1} | x_t) = N(x_{t-1}; \mu_\theta(X_t, t), \Sigma(x_t, t)) \quad (18)$$

where $\Sigma(x_t, t) = \tilde{\beta}_t \mathbf{I}$. From the above process we can find the image at moment $t-1$ with x_t known as:

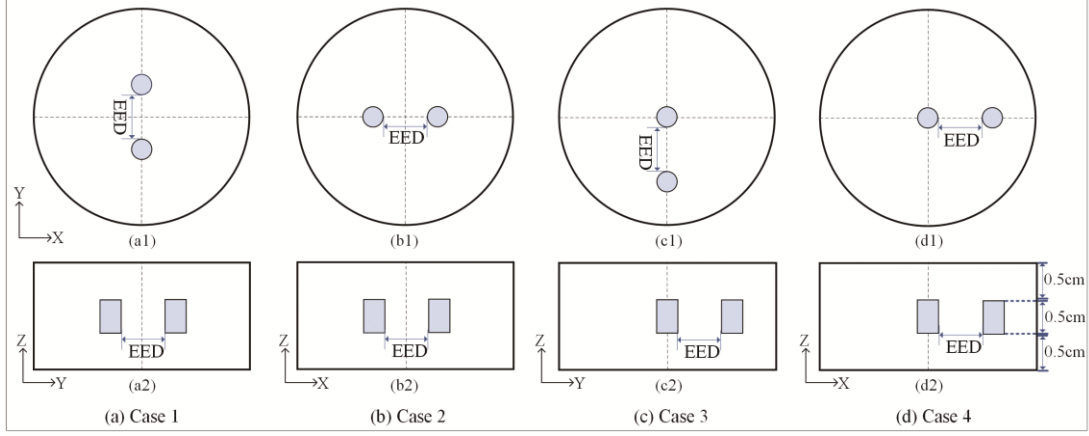


Figure 2: Experimental setup in the numerical simulation for four different cases.

$$x_{t-1} = \frac{1}{\sqrt{\alpha_t}} \left(x_t - \frac{1-\alpha_t}{\sqrt{1-\alpha_t}} \epsilon_\theta(X_t, t) \right) + \tilde{\beta}_t^{\frac{1}{2}} z \quad z \sim N(0, \mathbf{I}) \quad (19)$$

Sampling Process

For the sampling process, the fluorescence signals Φ_c is used as a conditional image to generate the FMT reconstructed image from the random noise image. Specifically, X_T is first obtained according to equation (15), and then the reconstructed 3D fluorescence image x_{rec} is obtained by iterating T -steps through equation (19). The sampling algorithm proceeds as shown in Algorithm 2.

Diff-FMT Preparation, Optimization and Evaluation

All experiments on the proposed Diff-FMT and the compared 3D-CNN (Guo et al., 2019) were run on a desktop computer equipped with an NVIDIA GeForce RTX 4090 with 24 RAM, Python version 3.10, and PyTorch version 2.1.1. Diff-FMT and 3D-CNN were trained using the same dataset and optimized using Adam gas pedal with learning rate set to 10^{-4} , batch size 32 and epoch 10000.

Preparation of the dataset

To verify the effectiveness of the proposed algorithm, we used a small dataset for network training. Specifically, we generated data by randomly adding fluorescent targets of different sizes and different optical properties. Different cylindrical fluorescent targets with random diameters varying from 1.3 to 1.7 mm and a fixed height of 5 mm were randomly located inside the phantoms. The horizontal and vertical coordinates of these fluorescent target centers were both randomly generated between -1.2 and 1.2 cm, and the edge-to-edge distances (EEDs) randomly varied from 0.3 to 5 mm. The source-detector configuration of the data was set to match that of the real experimental data. Finally, only 1,000 simulated small data samples were generated for training.

The independent test sets were used to test the optimal model.

Evaluation indicators

We use Dice (Chen et. al. 2014), contrast-to-noise ratio (CNR) (Zhang et. al. 2015b), and localization error (LE) (Guo et. al. 2019) to comprehensively assess the performance of Diff-FMT algorithm. The Dice coefficient is used to evaluate the similarity between the reconstructed region and the real fluorescence region. The larger the Dice, the closer the reconstructed fluorophore is to the real fluorophore. CNR is used to calculate the signal intensity difference between the region of interest (ROI) and the background region. The larger the CNR, the higher the image signal-to-noise ratio of the reconstructed image. LE calculates the localization error between the reconstructed region and the center of the real fluorescence region. The smaller the value, the higher the position accuracy of the reconstructed fluorophore.

Experimental Results

We conducted numerical simulation experiments to compare the reconstruction performance of 3D-CNN and Diff-FMT algorithms. A simulated cylinder with a radius and height of 1.5 cm is constructed, in which two fluorescent targets with a radius of 0.15 cm and a height of 0.5 cm at different positions are and excited with a point light source with a height of 0.75 cm. The XY planes and side planes of the dual fluorescent target at four different positions corresponding to four different cases are shown in Figure 2, and the EED values are 1 mm, 2 mm, 3 mm, respectively.

Comparison of Reconstruction Results

Symmetric Dual-Target Reconstruction Results

The reconstruction results of the symmetric fluorescent targets at different EEDs using Diff-FMT and 3D-CNN are shown in Figure 3. The first to the third rows are the results

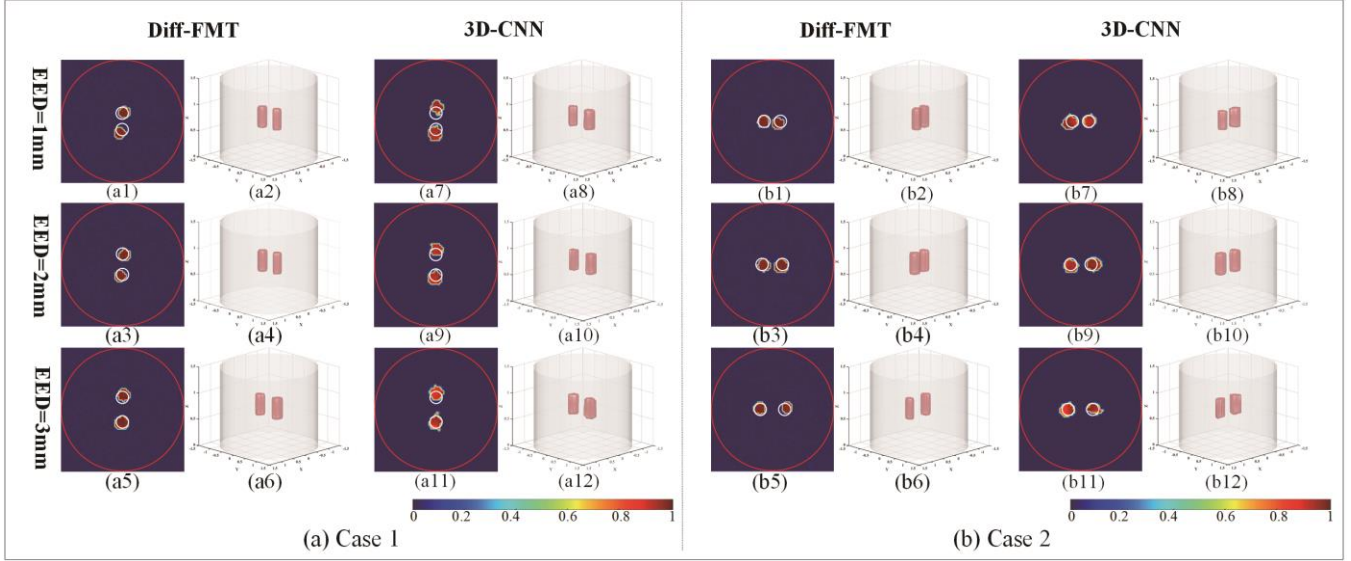


Figure 3: Numerical simulation reconstruction results of Diff-FMT and 3D-CNN for different EEDs (i.e., 1 mm, 2 mm, 3 mm). (a) XY planar slices and reconstructed 3D images of Case 1: Diff-FMT ((a1) - (a6)), 3D-CNN ((a7) - (a12)). (b) XY planar slice and reconstructed 3D image of Case 2: Diff-FMT((b1) - (b6)), 3D-CNN ((b7) - (b12)).

of 2D slices and 3D images at EED = 1 mm, EED = 2 mm, EED = 3 mm, respectively. The red circle represents the boundary of the numerical cylinder, and the white circle represents the position of the real fluorescent target.

As shown in Figure 3 (a), in Case 1, the shapes of the fluorophores reconstructed by 3D-CNN are all irregular. And when EED = 1 mm and 2 mm, 3D-CNN cannot accurately reconstruct the positions of the two fluorescent targets, and the position of one of the fluorophores reconstructed by 3D-CNN deviates more from the real one when EED is 3 mm. In contrast, better image restoration can be achieved by the Diff-FMT in two cases.

Table 1: Quantitative metrics for numerical simulation experiments of Case 1 and Case 2

Cases	Indexes Method	EED (mm)	CNR	LE (mm)		Dice
				S1	S2	
Case 1	Diff-FMT	1.00	9.57	0.11	0.23	0.50
		2.00	12.07	0.14	0.23	0.60
		3.00	13.34	0.18	0.18	0.64
	3D-CNN	1.00	6.78	0.23	0.20	0.41
		2.00	8.34	0.27	0.19	0.50
		3.00	12.07	0.25	0.20	0.61
Case 2	Diff-FMT	1.00	14.04	0.15	0.32	0.57
		2.00	16.13	0.26	0.20	0.69
		3.00	12.50	0.09	0.16	0.60
	3D-CNN	1.00	14.17	0.20	0.18	0.61
		2.00	13.49	0.17	0.18	0.70
		3.00	15.16	0.17	0.12	0.72

To more accurately assess the performance of different algorithms in terms of localization accuracy and shape recovery, we quantitatively evaluated the results reconstructed by the two algorithms, as shown in Table 1. From the results, it can be seen that the LE of Diff-FMT is overall lower, indicating that the positions of the fluorophores reconstructed by the proposed algorithm are more accurate compared to 3D-CNN. In addition, the CNR and Dice of Diff-FMT are overall higher than that of 3D-CNN, which indicates that the proposed algorithm performs better in terms of fluorescent target recovery effect and target shape accuracy. In particular, the proposed Diff-FMT algorithm has higher CNR (9.57 Vs 6.78 when EED = 1 mm) and Dice (0.5 Vs 0.41 when EED = 1 mm) than 3D-CNN for all EEDs in Case 1, indicating that the Diff-FMT is highly robust.

Table 2: Quantitative metrics for numerical simulation experiments of Case 3 and Case 4

Cases	Indexes Method	EED (mm)	CNR	LE (mm)		Dice
				S1	S2	
Case 3	Diff-FMT	1.00	12.10	0.31	0.22	0.50
		2.00	15.24	0.13	0.07	0.71
		3.00	13.52	0.20	0.16	0.64
	3D-CNN	1.00	5.88	0.34	0.18	0.16
		2.00	4.53	0.34	0.24	0.18
		3.00	4.42	0.34	0.21	0.29
Case 4	Diff-FMT	1.00	15.30	0.18	0.17	0.62
		2.00	15.65	0.13	0.19	0.72
		3.00	9.91	0.11	0.10	0.57
	3D-CNN	1.00	5.66	0.31	0.28	0.07
		2.00	5.36	0.31	0.26	0.04
		3.00	3.75	0.27	0.26	0.11

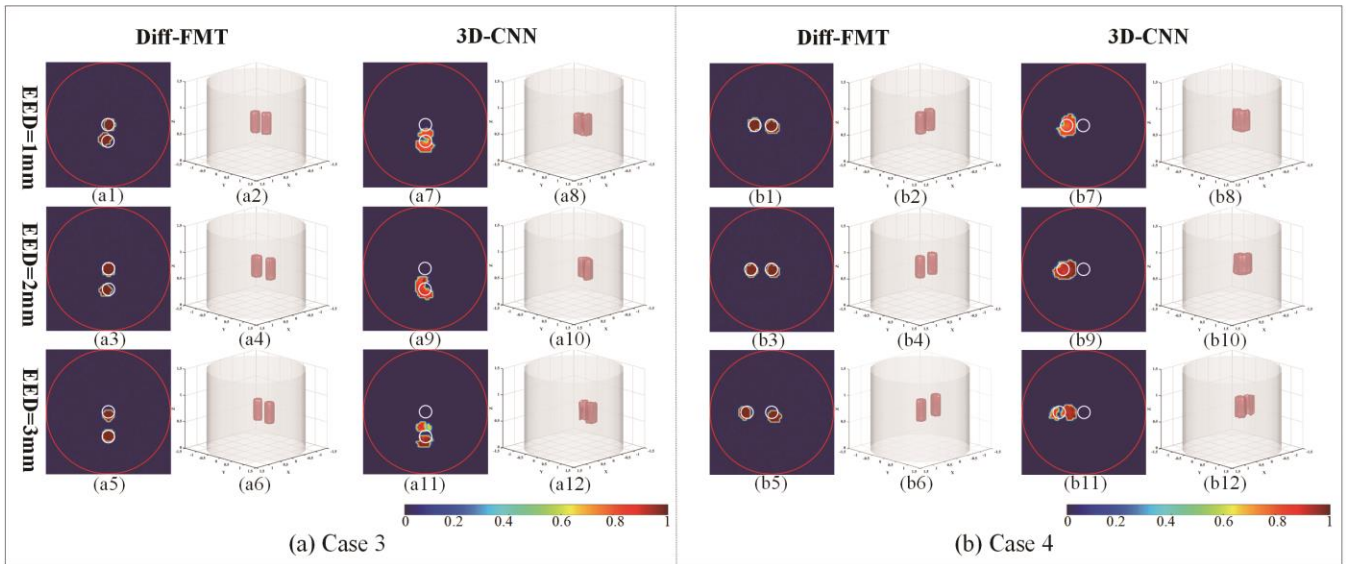


Figure 4: Numerical simulation reconstruction results of Diff-FMT and 3D-CNN for different EEDs (i.e., 1 mm, 2 mm, 3 mm). (a) XY planar slices and reconstructed 3D images of Case 3: Diff-FMT ((a1) - (a6)), 3D-CNN ((a7) - (a12)). (b) XY planar slice and reconstructed 3D image of Case 4: Diff-FMT((b1) - (b6)), 3D-CNN ((b7) - (b12)).

Asymmetric Dual-targets Reconstruction Results

In order to test the performance of the Diff-FMT algorithm in more complex experimental environments, we conducted reconstruction experiments of asymmetric fluorescent targets under different EEDs, and the reconstruction results using Diff-FMT and 3D-CNN are shown in Figure 4. As can be seen from the images in the XY plane and the 3D results, the performance of 3D-CNN is severely degraded in asymmetric dual-target reconstruction. In Case 3 and Case 4, when EED = 3 mm, the two fluorophores reconstructed by 3D-CNN are irregularly shaped and completely out of position, and the fluorophores reconstructed by the algorithm even appear to have edges that cannot be separated when EED = 1 mm and 2 mm. In contrast, the Diff-FMT algorithm obtained two fluorophores with more precise positions and regular shapes in all cases. This result indicates that Diff-FMT algorithm can still maintain its high performance in complex environments, showing superior robustness and adaptability.

The quantitative analysis of the Case 3 and Case 4 reconstruction results is shown in Table 2. It can be found that the CNR (In Case 3, 15.24 Vs 4.53 when EED = 2 mm) and Dice (In Case 3, 0.71 Vs 0.18 when EED = 2 mm) of Diff-FMT are significantly higher than those of 3D-CNN at different EEDs, indicating that Diff-FMT algorithm reconstructs fluorophores with higher contrast and a shape closer to the actual fluorescent target than 3D-CNN. In addition, except for the second fluorophore in Case 3 with EED = 1 mm, which has a larger LE value than 3D-CNN (0.22 Vs 0.18), the LE of Diff-FMT is lower in all other cases (Fluorophore S2 in Case 3: 0.07 Vs 0.24 when EED = 2 mm), which suggests that Diff-FMT's reconstructed fluorophore localization

accuracy is higher. From the above experimental results, with only 1000 training samples, Diff-FMT not only reconstructs better quality fluorophores compared to 3D-CNN, but also maintains high performance in more complex numerical simulation experiments.

Conclusion

In this paper, we propose a diffusion model-based Diff-FMT network model for FMT reconstruction. This model is different from previous deep learning algorithms that rely heavily on large-scale high-quality datasets. Instead, it uses the probability sampling mechanism of DDPM to extract image features in a progressive manner. In addition, the fluorescence signal is introduced as a condition to obtain the corresponding high-quality 3D fluorescence image. Preliminary experimental results show that Diff-FMT can generate high-quality 3D fluorescence images with a smaller amount of training data.

References

- Cao, C. G.; Xiao, A.; Cai, M. S.; Shen, B. L.; Guo, L. S.; Shi, X. J.; J, T.; and Hu, Z. H. 2022. Excitation-based fully connected network for precise NIR-II fluorescence molecular tomography. *Biomedical Optics Express* 13(12): 6284-6299. doi.org/10.1364/BOE.474982.
- Chen, C.; Tian, F. H.; Liu, H. L.; and Huang, J. Z. 2014. Diffuse optical tomography enhanced by clustered sparsity for functional brain imaging. *IEEE transactions on medical imaging* 33(12): 2323-2331. doi.org/10.1109/TMI.2014.2338214.
- Cheng, J. J.; and Luo, J. W. 2020. Tikhonov-regularization-based

- projecting sparsity pursuit method for fluorescence molecular tomography reconstruction. *Chinese Optics Letters* 18(1): 69-74. doi.org/10.3788/COL202018.011701.
- Chen, Y.; Du, M. F.; Zhang, J.; Zhang, G.; Su, L. Z.; Li, K.; Zhao, F. J. Yi, H. J.; Wang, L.; and Cao, X. 2023. Generalized conditional gradient method with adaptive regularization parameters for fluorescence molecular tomography. *Optics Express* 31(11): 18128-18146. doi.org/10.1364/OE.486339.
- Guo, H. B.; Yu, J. J.; He, X. W.; Hou, Y. Q.; Dong, F.; and Zhang, S. L. 2015. Improved sparse reconstruction for fluorescence molecular tomography with L 1/2 regularization. *Biomedical optics express* 6(5):1648-1664. doi.org/10.1364/BOE.6.001648.
- Guo, L.; Liu, F.; Cai, C. J.; Liu, J.; and Zhang, G. L. 2019. 3D deep encoder-decoder network for fluorescence molecular tomography. *Optic letters* 44(8): 1892-1895. doi.org/10.1364/OL.44.001892.
- Han, D.; Tian, J.; Zhu, S. P.; Feng, J. C.; Qin, C. H.; Zhang, B.; and Yang, X. 2010. A fast reconstruction algorithm for fluorescence molecular tomography with sparsity regularization. *Optics express* 18(8): 8630-8646. doi.org/10.1364/OE.18.008630.
- Han, H. H.; Tian, H.; Zang, Y.; Sedgwick, A. C.; Li, J.; Sessler, J. L.; He X P.; and James, T. D. 2021. Small-molecule fluorescence-based probes for interrogating major organ diseases. *Chemical Society Reviews* 50(17): 9391-9429. doi.org/10.1039/d0cs01183e.
- He, K. M.; Zhang, X. Y.; Ren, S. Q.; and Sun, J.; 2016. Deep residual learning for image recognition. In Proceedings of the IEEE conference on computer vision and pattern recognition. Las Vegas: IEEE Computer Society. doi.org/10.1109/cvpr.2016.90.
- He, Z. X.; Zhang, L.; Xing, L. X.; Sun, W. J.; Gao, X. J.; Zhang, Y. Q.; and Gao, F. 2024. IR780-based diffuse fluorescence tomography for cancer detection. *Journal of Biophotonics* 17(5): 1-12. doi.org/10.1002/jbio.202300493.
- Ho, J.; Jain, A.; and Abbeel, P. 2020. Denoising Diffusion Probabilistic Models. arXiv:2006.11239.
- Hua, Y. Z.; Jiang, Y. X.; Liu, K. X.; Luo, Q. M.; and Deng, Y. 2022. Interpretable model-driven projected gradient descent network for high-quality fDOT reconstruction. *Optics Letters* 47(10): 2538-2541. doi.org/10.1364/OL.459456.
- Jiang, Y. X.; Liu, K. X.; Li, W. S.; Luo, Q. M.; & Deng, Y. 2023. Deep background-mis modeling-learned reconstruction for high-accuracy fluorescence diffuse optical tomography. *Optics Letters* 48(13): 3359-3362. doi.org/10.1364/OL.490108.
- Li, C.; Zhou, S. S.; Chen, J.; and Jiang, X. Q. 2023. Fluorescence Imaging of Inflammation with Optical Probes. *Chemical and Biomedical Imaging* 1(6): 495-508. doi.org/10.1021/cbmi.3c00039.
- Liu, K.; Jiang, Y.; Li, W.; Chen, H.; Luo, Q.; & Deng, Y. 2023. High-fidelity mesoscopic fluorescence molecular tomography based on SSB-Net. *Optics Letters* 48(2): 199-202. doi.org/10.1364/OL.475949.
- Luo, X. L.; Ren, Q. Q.; Zhang, H.; Chen, C.; Yang, T.; He, X. W.; and Zhao, W. 2023. Efficient FMT reconstruction based on L1- α L2 regularization via half-quadratic splitting and a two-probe separation light source strategy. *Journal of the Optical Society of America A* 40(6): 1128-1141. doi.org/10.1364/JOSAA.481330.
- Meng, H.; Gao, Y.; Yang, X.; Wang, K.; and Tian, J. 2020. K-nearest neighbor based locally connected network for fast morphological reconstruction in fluorescence molecular tomography. *IEEE transactions on medical imaging* 39(10): 3019-3028. doi.org/10.1109/TMI.2020.2984557.
- Ntziachristos, V.; Tung, C. H.; Bremer, C.; Weissleder R. 2002. Fluorescence molecular tomography resolves protease activity in vivo. *Nature Medicine* 8: 757-761. doi.org/10.1038/nm729.
- Ntziachristos, V.; Schellenberger, E. A.; Ripoll, J.; Yessayan, D.; Graves, E.; Bogdanov Jr, A.; Josephson L.; Weissleder, R. 2004. Visualization of antitumor treatment by means of fluorescence molecular tomography with an annexin V-Cy5.5 conjugate. *Proceedings of the National Academy of Sciences* 101(33): 12294-12299. doi.org/10.1073/pnas.040113710.
- Soubret, A.; Ripoll, J.; and Ntziachristos, V. 2005. Accuracy of fluorescent tomography in the presence of heterogeneities: study of the normalized Born ratio. *IEEE transactions on medical imaging* 24(10): 1377-1386. doi.org/10.1109/TMI.2005.857213.
- Stuker, F.; Ripoll, J.; and Rudin, M. 2011. Fluorescence molecular tomography: principles and potential for pharmaceutical research. *Pharmaceutics*, 3(2): 229-274. doi.org/10.3390/pharmaceutics3020229.
- Sun, W. J.; Zhang, L. M.; Xing, L. X.; He, Z. X.; Zhang, Y. Q.; and Gao, F. 2024. Projected algebraic reconstruction technique-network for high-fidelity diffuse fluorescence tomography reconstruction. *Journal of the Optical Society of America A* 41(6): 988-999. /doi.org/10.1364/JOSAA.517742.
- Vaswani, A.; Shazeer, N.; Parmar, N.; Uszkoreit, J.; Jones, L.; Gomez, A. N.; Kaiser, L.; and Polosukhin, I. 2017. Attention is all you need. In Advances in Neural Information Processing Systems 30. New York: Curran Associates, Inc. doi.org/10.5555/3295222.3295349.
- Willmann, J. K.; Van Bruggen, N.; Dinkelborg, L. M.; and Gambhir, S. S. 2008. Molecular imaging in drug development. *Nature reviews Drug discovery* 7(7): 591-607. doi.org/10.1038/nrd2290.
- Wu, Y.; He, X. L.; Chen, Z. H.; Wei, X.; Liu, Y. Q.; Li, S. C.; Zhang, H. Yu, J. J. Guo, H. B. and He, X. W. 2024. Group sparse-based Taylor expansion method for liver pharmacokinetic parameters imaging of dynamic fluorescence molecular tomography. *Physics in Medicine and Biology* 69(11): 115006. doi.org/10.1088/1361-6560/ad4084.
- Xie, W. H.; Deng, Y.; Wang, K.; Yang, X. Q.; and Luo, Q. M. 2014. Reweighted L1 regularization for restraining artifacts in FMT reconstruction images with limited measurements. *Optics letters* 39(14): 4148-4151. doi.org/10.1364/OL.39.004148.
- Yang, Y.; Wan, W. B.; and Zhou, H. L. 2022. A model-driven deep unfolding network for fluorescence molecular tomography reconstruction. In Proceedings of Optics in Health Care and Biomedical Optics XII. online: SPIE. doi.org.10.1117/12.2643966.
- Yuan, Y. T.; Yi, H. J.; Kang, D. Z.; Yu, J. J.; Guo, H. B.; He, X. L.; and He, X. W. 2023. Robust transformed l1 metric for fluorescence molecular tomography. *Computer methods and programs in biomedicine* 234: 107503. doi.org/10.1016/j.cmpb.2023.107503.
- Zhang, G. L.; Pu, H. S.; He, W.; Liu, F.; Luo, J. W.; and Bai, J. 2015. Bayesian framework based direct reconstruction of fluorescence parametric images. *IEEE transactions on medical imaging* 34(6):1378-1391. doi.org/10.1109/TMI.2015.2394476.
- Zhang, G. L.; Pu, H. S.; He, W.; Liu, F.; Luo, J. W.; and Bai, J. 2015. Full-direct method for imaging pharmacokinetic parameters in dynamic fluorescence molecular tomography. *Applied Physics Letters* 106(8). doi.org/10.1063/1.4913690.
- Zhang, P.; Fan, G. D.; Xing, T. T.; Song, F.; Zhang, G. L. 2021. UHR-DeepFMT: Ultra-High Spatial Resolution Reconstruction of Fluorescence Molecular Tomography Based on 3-D Fusion Dual-

Sampling Deep Neural Network. *IEEE Trans Med Imaging* 40(11): 3217-3228. doi.org/10.1109/TMI.2021.3071556.

Zhang, X. X.; Jia, Y. F.; Cui, J. P.; Zhang, J.; Cao, X.; Zhang, L.; and Zhang, G. L. 2023. Two-stage deep learning method for sparse-view fluorescence molecular tomography reconstruction. *Journal of*

the Optical Society of America A 40(7): 1359-1371. doi.org/10.1364/JOSAA.489702.